HIGH POWER LASER
SCIENCE AND ENGINEERING

RESEARCH ARTICLE

Numerical study of spatial chirp distortion in quasi-parametric chirped-pulse amplification

Yirui Wang [1], Jing Wang [1], Jingui Ma [1], Peng Yuan[1], and Liejia Qian[1,2]

[1] *School of Physics and Astronomy, Shanghai Jiao Tong University, Shanghai 200240, China*

[2] *Tsung-Dao Lee Institute, Shanghai Jiao Tong University, Shanghai 200240, China*

Abstract

Optical parametric chirped-pulse amplification is inevitably subject to high-order spatial chirp, particularly under the condition of saturated amplification and a Gaussian pump; this corresponds to an irreversible spatiotemporal distortion and consequently degrades the maximum attainable focused intensity. In this paper, we reveal that such spatial chirp distortion can be significantly mitigated in quasi-parametric chirped-pulse amplification (QPCPA) with idler absorption. Simulation results show that the quality of focused intensity in saturated QPCPA is nearly ideal, with a spatiotemporal Strehl ratio higher than 0.98. As the seed bandwidth increases, the idler absorption spectrum may not be uniform, but the Strehl ratio in QPCPA can be still high enough due to stronger idler absorption.

Keywords: gain saturation; quasi-parametric chirped-pulse amplification; spatiotemporal distortions

1. Introduction

Ultrashort ultra-intense laser pulses have delivered peak intensities of 10^{22}–10^{23} W/cm^2 that represents the strongest radiation in the laboratory and enables the experimental research of extreme high-field physics[1–3]. However, ultrashort pulses with broad bandwidths are prone to spatiotemporal couplings (STCs)[4–7]. That is, there exists an interdependence between the temporal (or spectral) and spatial (or angular) properties of electromagnetic fields[8]. One of the simplest first-order STCs in space and time has a mathematical description of $E(x, t + \xi x)$ where ξ is the linear coupling coefficient. Since first-order STCs can be produced and compensated through angular-dispersion devices, they have been widely used to construct a pulse stretcher and compressor for chirped-pulse amplification (CPA)[9–16]. For example, in a pulse stretcher consisting of four prisms, the angular dispersion induced by the first prism is completely compensated in the second prism, which is anti-parallel to the first one, resulting in laser pulses with a pure temporal chirp at the output[11]. However, it is non-trivial to

compensate all the STCs introduced during the pulse propagation and amplification. For example, the misalignment of the gratings in either the stretcher or compressor results in residual couplings (also termed spatiotemporal distortions), including both first-order STCs and complicated high-order STCs. It has been experimentally demonstrated that the high-order STCs in imperfect compression are very difficult to be compensated and contribute to most of the spatiotemporal distortions of the compressed and focused signal[12,17–21].

The STC issue is pronounced in optical parametric chirped-pulse amplification (OPCPA) due to the nonlinear nature of parametric gain[4,22–27]. The spatiotemporal distortions acquired by the signal in the OPCPA amplifier do exist and will affect the compression and focusing of the output signal, even if the spatiotemporal distortions introduced by the stretcher, compressor and other chromatic optics can be perfectly removed. So far, the first-order distortions arising in the regime of small-signal amplification have been experimentally expounded and eliminated. Firstly, Bromage *et al.*[22] revealed that STC distortion in the form of angular dispersion vanishes when the OPCPA operates in the geometry of 'magic' phasematching. Besides, Zaukevičius *et al.*[23] demonstrated that STC distortions in the forms of spatial chirp and pulse-front tilt can be eliminated by pulse-front matching

Correspondence to: J. Wang, School of Physics and Astronomy, Shanghai Jiao Tong University, Shanghai 200240, China. Email: wangj1118@sjtu.edu.cn

1

between the pump and the signal. Nevertheless, a saturated OPCPA amplifier will introduce complicated spatiotemporal distortion in the form of high-order spatial chirp because of the back-conversion effect[26,27]. Such spatial chirp distortion cannot be compensated afterward and its prevention needs complicated shaping techniques of the pump pulse and beam. A numerical study by Giree *et al.*[26] proved that the spatial chirp distortion leads to a significant reduction in the spatiotemporal Strehl ratio (SR), which is the quality factor describing the degradation of focused peak intensity. Their simulations showed an SR decrease of more than 30% in saturated OPCPA.

Recently, quasi-parametric chirped-pulse amplification (QPCPA), a variant of OPCPA, has been proposed as a promising approach for enhancing the signal efficiency and gain bandwidth[28,29]. Conventional OPCPA adopts a nonlinear crystal that is transparent to all the interacting waves of the pump, signal and idler, whereas QPCPA employs a specific crystal with strong idler absorption. Since the idler absorption inhibits the detrimental effect of back-conversion, QPCPA can be made much more efficient and broadband than OPCPA. Because the only difference between OPCPA and QPCPA is the nonlinear crystal, QPCPA has broad prospects in applications such as a replacement in high-power OPCPA lasers. In this paper, we numerically demonstrate that the spatial chirp distortion can be minimized in the saturated QPCPA with a Gaussian-shaped pump. With idler dissipation, the signal of QPCPA behaves like those of energy-level amplifiers (e.g., Ti:sapphire laser) and the spatial chirp distortion inherent to OPCPA can thus be circumvented.

2. Numerical model

A comparative study on the spatial chirp distortion in non-collinear OPCPA and QPCPA is conducted based on solving a similar set of nonlinear coupled-wave equations[30] that describe the amplitude evolutions of the signal, idler and pump (A_s, A_i and A_p, respectively):

$$\frac{\partial A_i}{\partial z} + \sum_{n=1}^{\infty} \frac{(-1)^{n-1}}{n!} k^{(n)} \frac{\partial^n A_i}{\partial t^n} + \frac{i}{2k_i} \frac{\partial^2 A_i}{\partial x^2} + \rho_i \frac{\partial A_i}{\partial x}$$
$$= i\frac{\omega_i d_{\text{eff}}}{n_{ic}} A_p A_s^* e^{i\Delta kz} - \frac{\alpha_i}{2} A_i,$$

$$\frac{\partial A_s}{\partial z} + \sum_{n=1}^{\infty} \frac{(-1)^{n-1}}{n!} k^{(n)} \frac{\partial^n A_s}{\partial t^n} + \frac{i}{2k_s} \frac{\partial^2 A_s}{\partial x^2} + \rho_s \frac{\partial A_s}{\partial x}$$
$$= i\frac{\omega_s d_{\text{eff}}}{n_{sc}} A_p A_i^* e^{i\Delta kz},$$

$$\frac{\partial A_p}{\partial z} + \sum_{n=1}^{\infty} \frac{(-1)^{n-1}}{n!} k^{(n)} \frac{\partial^n A_p}{\partial t^n} + \frac{i}{2k_p} \frac{\partial^2 A_p}{\partial x^2} + \rho_p \frac{\partial A_p}{\partial x}$$
$$= i\frac{\omega_p d_{\text{eff}}}{n_{pc}} A_s A_i e^{-i\Delta kz}. \tag{1}$$

Numerical simulations of OPCPA and QPCPA are characterized by the idler absorption coefficients $\alpha_i = 0$ and $\alpha_i \neq 0$, respectively. The second terms on the left-hand side, that is, the $k^{(n)}$-terms, indicate the nth order dispersion of the crystal. The third and fourth terms represent the spatial diffraction and spatial walk-off, respectively. Here, $\rho_{s,i,p}$, $\omega_{s,i,p}$ and $n_{s,i,p}$ refer to the non-collinear angle including the birefringent walk-off, angular frequency and refractive index for signal, idler and pump waves, respectively, $\Delta k = k_p - k_s - k_i$ is the phase mismatch among the interacting waves, d_{eff} is the effective nonlinear coefficient and c is the speed of light in a vacuum.

By solving these equations under the assumption of pump non-depletion, the small signal gain for QPCPA can be given by the following:

$$g = \sqrt{g_0^2 + \frac{\alpha_i^2}{16} - \frac{\Delta k^2}{4}} - \frac{\alpha_i}{4}, \quad \text{with } g_0 = \sqrt{\frac{2\omega_s \omega_i d_{\text{eff}}^2 I_{p0}}{\varepsilon_0 n_s n_i n_p c^3}}, \tag{2}$$

where I_{p0} is the pump intensity and ε_0 is the vacuum permittivity. Obviously, the idler absorption enhances the tolerance of small signal gain to Δk and thus reduces the impact of Δk on the quasi-parametric amplification.

When the QPCPA falls in the saturation regime, its self-phase-locking characteristic[29] makes the direction of energy flow unchanged and the signal continues to extract energy from the pump. Theoretically, the pump-to-signal energy conversion efficiency can reach the quantum limit of ω_s/ω_p. The spatiotemporal intensity profile of the output chirped signal can thus be approximately deduced as follows:

$$I_s(x,t) = \frac{\omega_s}{\omega_p} I_p(x,t). \tag{3}$$

Equation (3) indicates that the spatial and temporal profiles of the output signal depend only on the shape of the pump. Clearly, the dependence of amplified spectra on transverse spatial positions is fundamentally mitigated in the QPCPA scheme.

The impact of spatiotemporal distortions on the focused peak intensity reduction can be characterized by the spatiotemporal SR of the amplified signal beam. The SR is numerically defined as follows[26]:

$$\text{SR} = \frac{\max\left\{\left|\iint a(x,\omega)\exp(-ik_x x)\exp(i\omega t)\,\mathrm{d}x\mathrm{d}\omega\right|^2\right\}}{\max\left\{\left|\iint \mu\sum_\omega a(x,\omega)\sum_x a(x,\omega)\exp(-ik_x x)\exp(i\omega t)\,\mathrm{d}x\mathrm{d}\omega\right|^2\right\}}, \tag{4}$$

where $a(x,\omega)$ represents the field of the compressed amplified signal beam with spatiotemporal distortions, $\sum_\omega |a(x',\omega)| \sum_x |a(x,\omega')|$ represents the distortion-free field constructed from $a(x,\omega)$ and μ is an adaptive constant
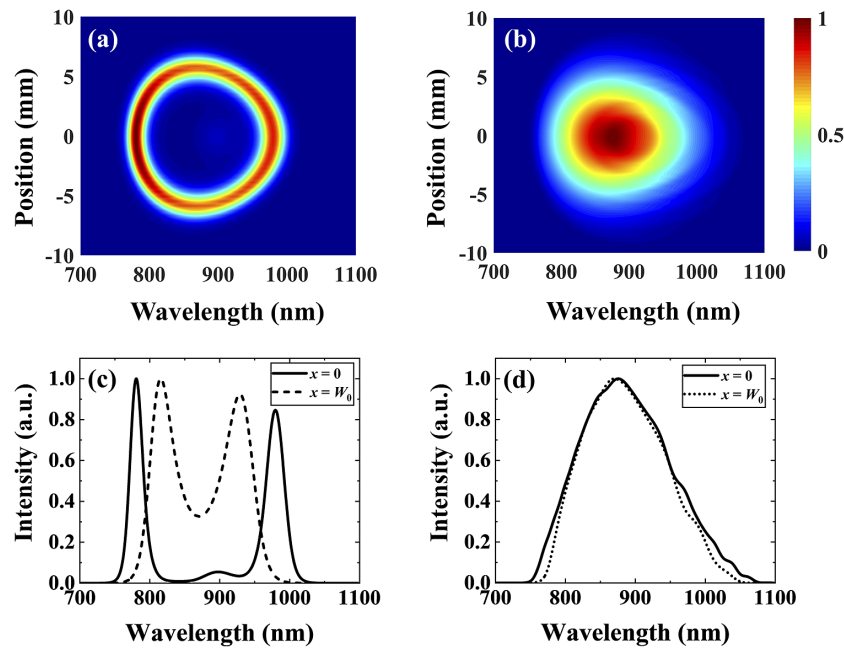
Figure 1. Comparison of the spatial chirp distortion of the amplified signal calculated for (a), (c) saturated OPCPA based on a 5-mm-thick YCOB crystal and (b), (d) saturated QPCPA based on a 15-mm-thick Sm^{3+}:YCOB crystal. (a), (b) Intensity profiles in the spatial and spectral domain. (c), (d) Signal spectra at the beam center ($x = 0$) and beam edge ($x = W_0$).

that ensures energy conservation for both fields. The peak intensity at the focal plane is calculated through Fourier transformation. Equation (4) implies that a pulse with strong spatiotemporal distortions corresponds to a low SR.

3. Simulation results and discussion

The numerical simulation is performed in the (z, x, t) dimensions, where z is the propagation direction of the wave vector in crystals, x is the transverse position and t is the time. Non-collinear amplification geometry that supports broad gain bandwidth is adopted in the simulations. The first-order distortions are eliminated by the 'magic' phase-matching and pulse-front matching between the pump and the signal. The simulation parameters are as follows: the pump has a spatiotemporally Gaussian profile with a wavelength of 515 nm, a pulse duration of 1.5 ps, a beam waist of 5 mm and a peak intensity of 80 GW/cm^2; the signal is a spatiotemporally Gaussian chirped pulse with a pulse duration of 1 ps, a spectral bandwidth of 100 nm centered at 850 nm (corresponding to a 6.4-fs Fourier transform-limited pulse duration), a beam waist W_0 of 5 mm and a peak intensity of 0.8 GW/cm^2; the nonlinear crystals are Type-I YCOB (transparent to the idler wave, i.e., $\alpha_i = 0$ in Equation (1)) for OPCPA and Type-I Sm^{3+}:YCOB (an average idler absorption of $\alpha_i = 2$ cm^{-1}) for QPCPA. All the values of the bandwidth, beam width and pulse duration refer to their full width at half maximum (FWHM). The above simulation parameters of the pump and seed signal are typical for high-intensity picosecond-pumped OPCPA

systems[26,31]. For example, in the Petawatt Field Synthesizer (Max-Planck-Institut für Quantenoptik, Germany), the pump laser of OPCPA is a 515-nm picosecond laser with an intensity up to 100 GW/cm^2, which was produced by second-harmonic generation of a Joule-energy picosecond Yb:YAG thin-disk laser, and the ultrabroadband seed is the output of a few-cycle Ti:sapphire laser oscillator (Rainbow, Femtolasers), which had a pulse duration of 6 fs and a spectral coverage of 700–1400 nm.

To characterize the spatiotemporal distortions of amplified signals for saturated OPCPA (based on YCOB) and QPCPA (based on Sm^{3+}:YCOB), the lengths of YCOB and Sm^{3+}:YCOB were set to 5 and 15 mm, respectively. For OPCPA, 5-mm-thick YCOB corresponds to a conversion efficiency of approximately 10%, which leads to severe back-conversion at the signal beam center. For QPCPA, 15-mm-thick Sm^{3+}:YCOB corresponds to a stable high conversion efficiency (~42%) without back-conversion across the signal beam. Amplified signals from such saturated OPCPA and QPCPA are plotted in the spatial and spectral domains in the upper row of Figure 1. The back-conversion effect and wavelength-dependent amplification saturation in OPCPA can be clearly seen through the 2D signal distribution in space and the spectrum (Figure 1(a)). The ring-shaped signal profile implies a strong spatial chirp distortion. Specifically, the wavelength is a nonlinear function of the transverse spatial coordinate, that is

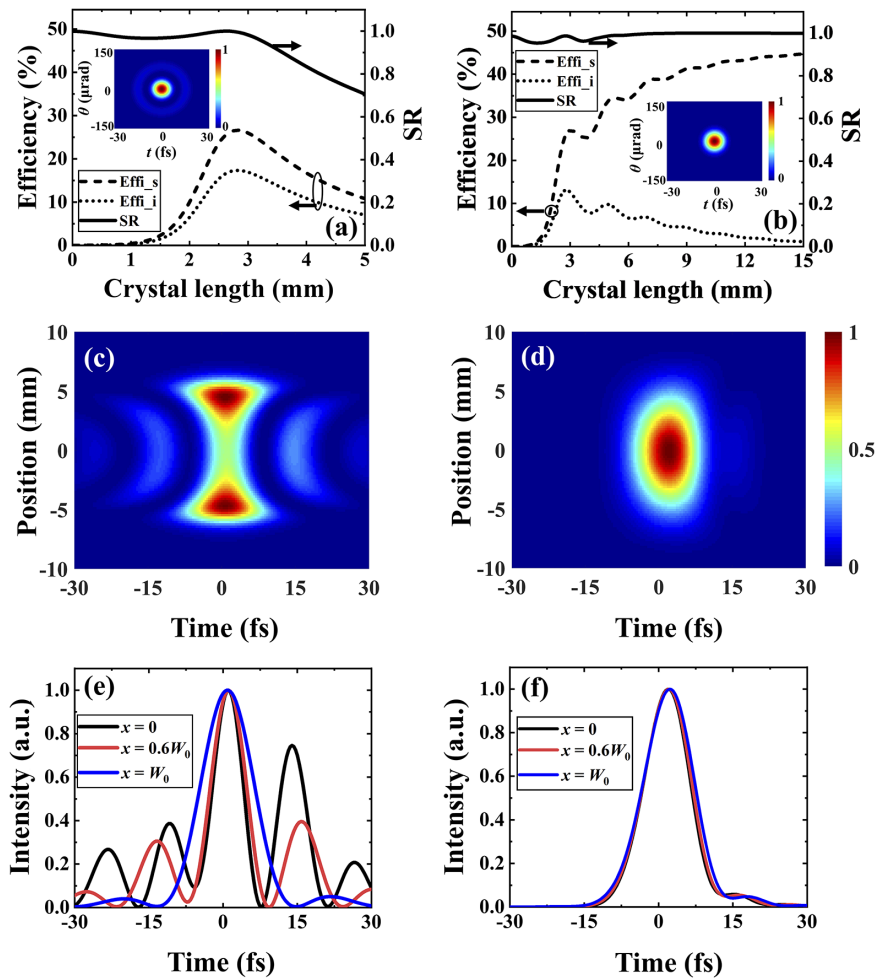$$\xi_{x\lambda} = \frac{\partial \lambda}{\partial x} \neq \text{const}, \qquad (5)$$

Figure 2. Comparison of the SR and spatiotemporal performance of OPCPA and QPCPA outputs. (a), (b) The evolutions of SR and signal efficiency with the crystal length. (c), (d) The compressed signal distribution in space and time. (e), (f) Three compressed signal pulses sampled at $x = 0$, $0.6W_0$ and W_0, for OPCPA and QPCPA, respectively. Insets in (a) and (b) depict the spatiotemporal profiles of the focused signal, which were calculated with the crystal lengths of 5 and 15 mm, respectively. Simulation parameters were the same as those listed in Figure 1.

where $\xi_{x\lambda}$ is the spatial chirp coefficient, which is symmetric about the beam center because of the Gaussian-shaped pump. The spatial chirp coefficient in OPCPA is small near the beam center and becomes larger away from the center. By contrast, the amplified signal in QPCPA exhibits a significantly smaller space–spectrum modulation (Figure 1(b)), which is thus more favorable to achieve higher focused intensity. This is because the idler absorption in the QPCPA crystal suppresses the back-conversion near the central wavelength, which consequently weakens the space-dependent spectral modulation. The signal spectra sampled at the beam center ($x = 0$) and edge ($x = W_0$) are shown in Figures 1(c) and 1(d). In OPCPA, the signal beam center with the highest pump intensity is the first to enter the gain saturation and causes the energy back-conversion from the signal and idler to the pump, which results in a central dip in the 2D signal distribution with two spectral peaks of 790 and 970 nm. At the signal beam edges of $x = \pm 5$ mm, the back-conversion effect is negligible because of the relatively

low pump intensity, and their spectra have a good shape but a smaller range of 810–940 nm. In contrast, in QPCPA (Figure 1(b)), all the spectral peaks from the beam center to the edge appear at nearly the same wavelength of 870 nm (i.e., $\xi_{x\lambda} = \partial\lambda/\partial x \approx 0$), indicating no spatial chirp distortion.

The SR evolutions with crystal length in OPCPA and QPCPA are shown by the solid curves in Figures 2(a) and 2(b), respectively. The pump-to-signal conversion efficiency (dashed curve) is also given to represent the degree of amplification saturation. The energy back-conversion from the signal and idler to the pump starts at the crystal length $z = 3$ mm. Notably, OPCPA suffers a remarkable SR decline from 1.0 to 0.7 in the regime of saturated amplification, which indicates a degree of spatial chirp distortion and a 30% reduction of the focused peak intensity. In contrast, the evolutions of SR and conversion efficiency are completely different in QPCPA. As the idler is continuously consumed due to crystal absorption (dotted curve), the energy back-conversion from the signal and idler to the pump is no
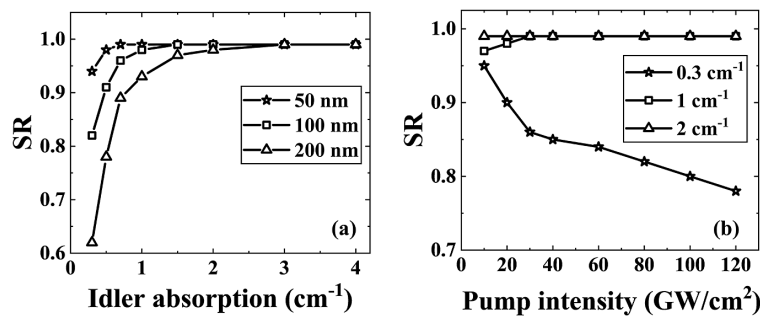
Figure 3. The dependence of SR performance on the idler absorption coefficient, seed bandwidth and pump intensity. (a) Calculated SR versus idler absorption coefficient for three seed bandwidths of 50, 100 and 200 nm under a fixed pump intensity of 80 GW/cm². (b) Calculated SR versus pump intensity for three idler absorption coefficients of 0.3, 1, and 2 cm⁻¹ under a fixed seed bandwidth of 100 nm.
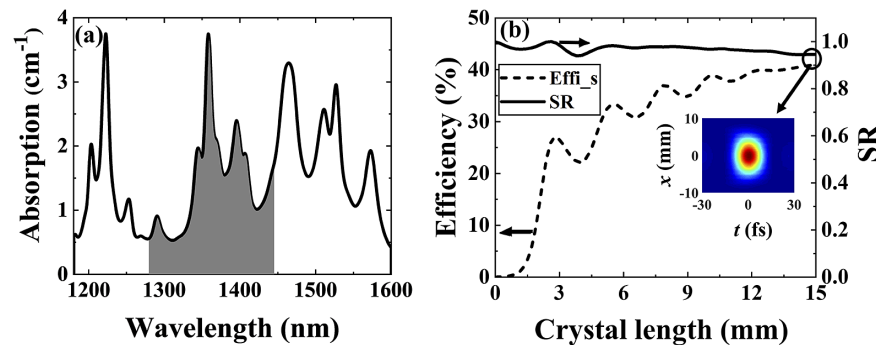

Figure 4. Characterization of the spatiotemporal performance of QPCPA based on a real Sm^{3+}:YCOB crystal. (a) The absorption spectrum of a real Sm^{3+}:YCOB crystal, where the gray area of the spectrum is adopted in the simulation of QPCPA. (b) The evolutions of SR and signal efficiency with the crystal length under the condition of nonuniform idler absorption. The inset shows the spatiotemporal distribution of the compressed signal, which was calculated with the crystal length of 15 mm.

longer significant. As a result, the SR in QPCPA remains at a high value of more than 0.98 and, meanwhile, the signal efficiency increases up to 42%. While a high-efficiency OPCPA always comes at the cost of SR reduction, the QPCPA scheme enables simultaneous high efficiency and high SR because of less spatial chirp distortion.

Owing to the severe spatial chirp distortion, the 2D signal distribution of OPCPA has several lobes with significant energy portions (Figure 2(c)). The spectral dip of the amplified signal at $x = 0$ leads to strong side pulses in the compressed pulses, as indicated in Figure 2(e). In addition, the compressed pulses at the beam edges have fewer side pulses. The presence of these side pulses in OPCPA also implies a substantial degradation in spatiotemporal focusability. By contrast, the compressed amplified signal output from QPCPA exhibits few STCs in its spatiotemporal intensity profile (Figure 2(d)), and the pulse durations at different beam positions are about 10 fs, similar to that of the seed (Figure 2(f)).

It is instructive to study the impact of idler absorption, pump intensity and seed bandwidth on the QPCPA performance in mitigating spatial chirp distortion. As illustrated in Figure 3(a), for fixed pump intensity and seed bandwidth, the SR is sensitive to idler absorption coefficient α_i only in the regime of weak absorption, while it becomes insensitive

to α_i once it exceeds a critical value. These results suggest that a uniform absorption across the idler spectrum is not necessary to achieve a high SR performance, which sets a loose requirement on the idler absorption of QPCPA crystals. Besides, the critical value of α_i to ensure an SR higher than 0.98 increases with the signal bandwidth. Concretely, for the pump intensity of 80 GW/cm² and the seed bandwidth of 50 nm, the critical α_i is 0.7 cm⁻¹. As the seed bandwidth increases to 100 and 200 nm, the critical α_i needs to be 1.5 and 3 cm⁻¹, respectively. Thus, a larger bandwidth QPCPA requires a stronger idler absorption to mitigate spatial chirp distortion and maintain good spatiotemporal performance. The dependence of critical α_i on seed bandwidth is reasonable because the edge frequency component of a broadband seed is subject to a larger phase mismatch and needs a stronger idler absorption to prevent the back-conversion effect, as revealed by Equation (2). On the other hand, for an idler absorption coefficient higher than 1 cm⁻¹, the consequent SR is also insensitive to the pump intensity, as shown in Figure 3(b). However, for an idler absorption coefficient as weak as 0.3 cm⁻¹, the resultant SR depends strongly on the pump intensity, like the situation for OPCPA.

In practice, the absorption coefficient is not always uniform across the idler spectrum. To study the spatiotemporal performance of QPCPA under nonuniform idler absorption,

we implemented the QPCPA simulation based on a real Sm^{3+}:YCOB crystal. Figure 4(a) plots the experimentally measured absorption spectrum of a real Sm^{3+}:YCOB crystal. For an 830-nm-centered seed signal with a 60-nm bandwidth and a 515-nm pump pulse, the idler covers a spectrum spanning from 1280 to 1440 nm, that is, the gray shaded area in Figure 4(a). The absorption coefficient within the selected spectrum varies from 0.5 to 3.7 cm^{-1}. Even under such a nonuniform idler absorption coefficient, the spatiotemporal intensity profile of the compressed signal shown in the inset of Figure 4(b) exhibits negligible STC distortion. As a result, when QPCPA operates in the regime of saturated amplification, the signal efficiency stabilizes around approximately 40% and the SR remains greater than 0.95. These results suggest that the nonuniform absorption spectrum of practical QPCPA crystals still has the QPCPA advantage of high spatiotemporal focusability.

4. Conclusion

In conclusion, we have numerically demonstrated that the spatial-chirp distortion inherent to saturated OPCPA can be overlooked in QPCPA. For a Gaussian-pumped OPCPA operating in the regime of saturated amplification, the back-conversion effect inevitably leads to a dramatic spatial chirp distortion. Hence, high conversion efficiency is achieved at the cost of degradation in the spatiotemporal focusability of the amplified signal (manifested by an SR much less than 1.0) in OPCPA. Based on a comparative study, we show that QPCPA naturally mitigates the spatial chirp distortion, and thereby high conversion efficiency and good spatiotemporal focusability (manifested by the SR close to 1.0) can be simultaneously achieved. Although the QPCPA performance in mitigating spatial-chirp distortion depends on the idler absorption exerted by the QPCPA crystal, a good SR close to 1.0 can be achieved for a wide range of idler absorption coefficients under a fixed pump intensity, as along as the idler absorption coefficient is higher than a critical value. For a pump intensity of 80 GW/cm^2 and a seed bandwidth of 50 nm, this critical absorption coefficient is as low as 0.7 cm^{-1}, which is easily satisfied in real QPCPA crystals. This critical absorption coefficient increases with the seed bandwidth. In addition, a seed bandwidth of 200 nm necessitates a critical absorption coefficient of 3 cm^{-1}. That is, relatively strong idler absorption is necessary for implementing ultrabroadband QPCPA. This paper suggests that QPCPA is prospective to minimize spatial chirp distortions without the need for pulse and beam shaping, and to achieve a further breakthrough in the attainable focused peak intensity.

Acknowledgment

Competing interests

The authors declare none.

References

1. N. C. Danson, C. Haefner, J. Bromage, and T. Butcher, High Power Laser Sci. Eng. **7**, e54 (2019).
2. J. Vyskočil, E. Gelfer, and O. Klimo, Plasma Phys. Controlled Fusion **62**, 064002 (2020).
3. J. W. Yoon, Y. G. Kim, I. W. Choi, J. H. Sung, H. W. Lee, S. K. Lee, and C. H. Nam, Optica **8**, 630 (2021).
4. A. Jeandet, S. W. Jolly, A. Borot, and B. Bussière, Opt. Express. **30**, 3262 (2022).
5. S. Akturk, X. Gu, P. Bowlan, and R. Trebino, J. Opt. **12**, 093001 (2010).
6. E. Gerstner, Nature **446**, 16 (2007).
7. I. Walmsley, L. Waxer, and C. Dorrer, Rev. Sci. Instrum. **72**, 1 (2001).
8. S. Akturk, X. Gu, P. Gabolde, and R. Trebino, Opt. Express **13**, 8642 (2005).
9. K. Osvay, A. P. Kovács, Z. Heiner, G. Kurdi, J. Klebniczki, and M. Csatári, IEEE J. Sel. Top. Quantum Electron. **10**, 213 (2004).
10. K. Varjú, A. P. Kovács, G. Kurdi, and K. Osvay, Appl. Phys. B **74**, s259 (2002).
11. I. V. Yakovlev, Quantum Electron. **44**, 393 (2014).
12. G. Pariente, V. Gallet, A. Borot, O. Gobert, and F. Quéré, Nat. Photonics **10**, 547 (2016).
13. Y. Chu, Z. Gan, X. Liang, and L. Yu, Opt. Lett. **40**, 5011 (2015).
14. J. H. Sung, H. W. Lee, J. Y. Yoo, and J. W. Yoon, Opt. Lett. **42**, 2058 (2017).
15. K. Nakamura, H. S. Mao, A. J. Gonsalves, and H. Vincenti, IEEE J. Quantum Electron. **53**, 1 (2017).
16. D. N. Papadopoulos, J. P. Zou, C. Le Blanc, and G. Chériaux, High Power Laser Sci. Eng. **4**, e34 (2016).
17. Z. Li, K. Tsubakimoto, H. Yoshida, Y. Nakata, and N. Miyanaga, Appl. Phys. Express **10**, 102702 (2017).
18. Z. Li and N. Miyanaga, Opt. Express **26**, 8453 (2018).
19. V. Leroux, S. W. Jolly, M. Schnepp, T. Eichner, S. Jalas, M. Kirchen, P. Messner, C. Werle, P. Winkler, and A. R. Maier, Opt. Express **26**, 13061 (2018).
20. A. Jeandet, A. Borot, K. Nakamura, and S. W. Jolly, J. Phys. Photonics **1**, 035001 (2019).
21. V. Leroux, T. Eichner, and A. R. Maier, Opt. Express **28**, 8257 (2020).
22. J. Bromage, C. Dorrer, and J. D. Zuegel, Opt. Lett. **35**, 2251 (2010).
23. A. Zaukevičius, V. Jukna, R. Antipenkov, V. Martinėnaitė, A. Varanavičius, A. P. Piskarskas, and G. Valiulis, J. Opt. Soc. Am. B **28**, 2902 (2011).
24. A. Shirakawa, I. Sakane, and T. Kobayashi, Opt. Lett. **23**, 1292 (1998).
25. O. Isaienko and E. Borguet, J. Opt. Soc. Am. B **26**, 965 (2009).
26. A. Giree, M. Mero, G. Arisholm, M. J. Vrakking, and F. J. Furch, Opt. Express **25**, 3104 (2017).
27. T. Eichner, T. Hülsenbusch, J. Dirkwinkel, T. Lang, L. Winkelmann, G. Palmer, and A. R. Maier, Opt. Express **30**, 3404 (2022).
28. J. Ma, J. Wang, P. Yuan, and G. Xie, Optica **2**, 1006 (2015).
29. J. Ma, J. Wang, B. Zhou, and P. Yuan, Opt. Express **25**, 25149 (2017).
30. G. Rustad, G. Arisholm, and Ø. Farsund, Opt. Express **19**, 2815 (2011).
31. A. Kessel, V. E. Leshchenko, O. Jahn, and M. Krüger, Optica **5**, 434 (2018).